

Beyond mean-field study of a binary bosonic mixture in a state-dependent honeycomb lattice

Lushuai Cao^{1,3}, Sven Krönke¹, Jan Stockhofe¹, Peter Schmelcher^{1,3}, Juliette Simonet², Klaus Sengstock^{1,2}, Dirk-Sören Lühmann²

¹ Zentrum für Optische Quantentechnologien, Universität Hamburg, Luruper Chaussee 149, D-22761 Hamburg, Germany

² Institut für Laserphysik, Universität Hamburg, Luruper Chaussee 149, D-22761 Hamburg, Germany

³ The Hamburg Centre for Ultrafast Imaging, Luruper Chaussee 149, D-22761 Hamburg, Germany

E-mail: lcao@physnet.uni-hamburg.de, sven.kroenke@physnet.uni-hamburg.de, jstockho@physnet.uni-hamburg.de, pschmelc@physnet.uni-hamburg.de, jsimonet@physik.uni-hamburg.de, ksengsto@physnet.uni-hamburg.de, dluhman@physnet.uni-hamburg.de

Abstract. We investigate a binary mixture of bosonic atoms loaded into a state-dependent honeycomb lattice. For this system, the emergence of a so-called twisted-superfluid ground state was experimentally observed in [Soltan-Panahi *et al.*, Nat. Phys. **8**, 71 (2012)]. Theoretically, the origin of this effect is not understood. We perform numerical simulations of an extended Bose-Hubbard model adapted to the experimental parameters employing the Multi-Layer Multi-Configuration Time-Dependent Hartree method for Bosons. Our results confirm the overall applicability of mean-field theory within the relevant parameter range. Beyond this, we provide a detailed analysis of correlation effects correcting the mean-field result. These have the potential to induce asymmetries in single shot time-of-flight measurements, but we find no indication of the patterns characteristic of the twisted superfluid. We comment on the restrictions of our model and possible extensions.

PACS numbers: 03.75.Hh, 67.85.Hj, 67.85.Fg

1. Introduction

The experimental realization of Bose-Einstein condensates (BECs) in dilute gases of alkali atoms in 1995 [1–3] has triggered extensive studies on ultracold atomic systems. Present day experimental techniques allow for highly precise control of ultracold atomic ensembles, including an almost perfect decoupling from the environment as well as a free design of the confining potential landscape [4, 5] and even tunability of the inter-atom interactions, via Feshbach [6–8] and confinement induced resonances [9–13]. This exceptional degree of controllability suggests to use ultracold atom systems for the purpose of quantum simulation. Phenomena to be potentially simulated with ultracold atoms in the laboratory come from fields as diverse as cosmology [14–17] or strongly correlated condensed matter systems [18–22], to name only a few. Importantly, internal (such as spin) degrees of freedom of the system to be simulated can be mimicked using different species of atoms. Such multi-species ultracold ensembles, including Bose-Bose [23, 24], Fermi-Fermi [25, 26] and even Bose-Fermi mixtures [27–31], have been extensively studied.

Among the various observations made in ultracold atomic mixtures, an intriguing observation of the so-called twisted superfluid (TSF) state is reported for a two-component bosonic mixture loaded into a state-dependent honeycomb lattice (SDHL) [32]. Experimentally, it is found that for a range of parameters of the SDHL potential the ground state of the binary atomic system has unusual properties, setting it apart from an ordinary superfluid phase. In such a lattice geometry, for a single spin state, the free-space momentum distribution displays a six-fold rotational symmetry in the first order Bragg peaks observed after time-of-flight. For a mixture of two spin states, two features characteristic for the TSF phase are observed in the quasi-momentum distribution:

- (P1) A reduced three-fold symmetry is observed for each spin state, appearing as an alternating pattern in the first-order momentum peaks. The six first order Bragg peaks can thus be grouped in two sets, each forming an equilateral triangle.
- (P2) It is furthermore observed that the two spin state show a complementary momentum distribution, populating different triangles. The six-fold symmetry expected for the lattice geometry is then restored in the summed momentum distribution of the two spin states.

Theoretically, the mechanism driving the emergence of such a TSF state is unclear. A recent mean-field study [33] did not find signatures of the type (P1) or (P2), speculating at the same time about the relevance of beyond mean-field effects. In this work, we aim to clarify this point by performing full many-body quantum simulations of an extended Bose-Hubbard model beyond the mean-field approximation to investigate the ground state of binary bosonic mixtures in the SDHL, looking in particular for the above TSF signatures. Our investigation shows that in the small lattice depth regime, where the emergence of TSF was found in the experiment [32], the system is indeed well described by mean-field theory. Correcting the mean-field approximation,

we observe inter-species quantum correlations with a weak but finite amplitude. We demonstrate that these correlations can modify the population distribution of the first order Bragg peaks in free-momentum space, however our findings do not confirm the presence of properties (P1) and (P2). These results indicate that within the lowest band extended Bose-Hubbard model the twisted superfluid effect cannot be ascribed to quantum correlation effects beyond mean-field. The main limitations of our analysis are the restriction to the lowest Bloch band and the finite domain size of the numerical simulations. Also higher order tunneling processes such as the density-induced tunneling [34] that are not contained in our Bose-Hubbard Hamiltonian might play a role.

The paper is organized as follows: in chapter 2 we briefly describe the experimental setup and the Hamiltonian corresponding to our theoretical model. The numerical method Multi-Layer Multi-Configuration Time-Dependent Hartree method for Bosons (ML-MCTDHB) is introduced in chapter 3. In chapter 4 we present the results of the simulations, and a summary as well as a discussion is given in chapter 5.

2. Setup

In the experiment [32], the ground state properties of binary bosonic mixtures loaded into a two-dimensional SDHL are investigated. The atomic samples consist of ^{87}Rb atoms in different spin states $|F, m_F\rangle$ from the hyperfine manifolds $F = 1, 2$ with Zeeman sublevels m_F . The atoms experience a state-dependent potential generated by the intersection of three coplanar linearly polarized laser beams at an angle of 120° , with the polarization of each laser beam lying in the intersection plane. The quantization axis of the system is defined by a homogeneous magnetic field. Orientating the magnetic field perpendicular to the lattice plane results in alternating circular polarization on lattice sites and thereby gives the following SDHL potential [34]:

$$V(\mathbf{x}) = -V_0[6 - 2 \sum_{i=1}^3 \cos(\mathbf{b}_i \mathbf{x}) + \sqrt{3}(-1)^F m_F \eta \sum_{i=1}^3 \sin(\mathbf{b}_i \mathbf{x})], \quad (1)$$

where V_0 and λ denote the lattice depth and laser wavelength, respectively. The vectors $\mathbf{b}_1 = \frac{2\pi}{\lambda}(\sqrt{3}, 0)$ and $\mathbf{b}_2 = \frac{2\pi}{\lambda}(-\frac{\sqrt{3}}{2}, \frac{3}{2})$ span the reciprocal Bravais lattice while $\mathbf{b}_3 = -\mathbf{b}_1 - \mathbf{b}_2$. The weight of the state-dependent term is given by the dimensionless constant $\eta = 0.13$ for the experimental values [34]. In the third spatial dimension, the atomic motion is frozen by a deep one-dimensional lattice, creating effectively a stack of planar samples taken to be fully decoupled from each other.

In the following we will focus on a bosonic mixture of the two spin states $|1, 1\rangle$ and $|1, -1\rangle$, denoted as \uparrow and \downarrow spins, for which the emergence of the TSF phase has been observed experimentally [32]. As shown for the \uparrow species in figure 1(a), the SDHL features a non-trivial unit cell of two, in general, inequivalent sites referred to as A and B: While the A/B sites correspond to deep/shallow sites for the \uparrow species, they exactly interchange their roles for the \downarrow species. We introduce $a = \frac{2}{3\sqrt{3}}\lambda$ denoting the distance between a neighboring A – B pair.

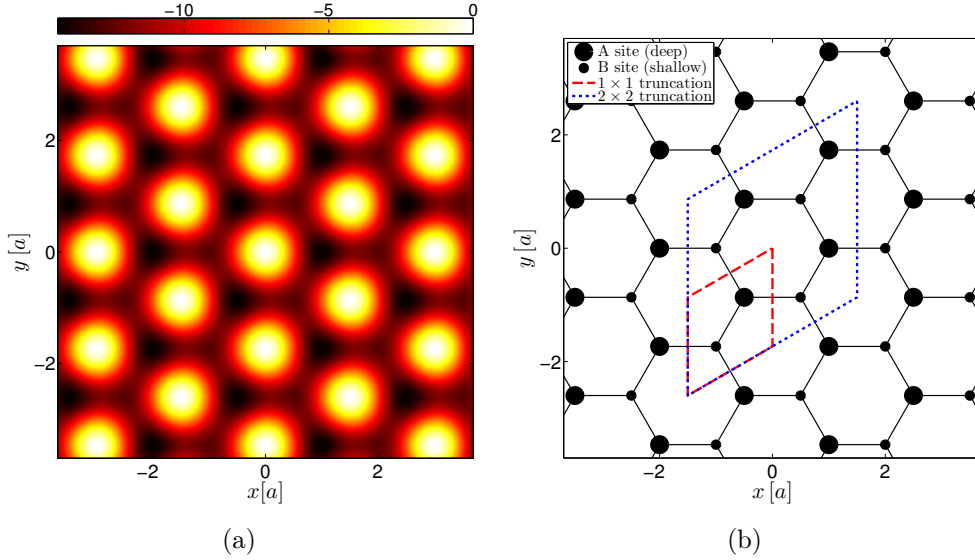


Figure 1. (a) The SDHL potential landscape $V(x, y)$ and (b) a schematic sketch of the lattice sites for \uparrow bosons. The potential in (a) is calculated from equation. (1) at a lattice depth $V_0 = 1.5 E_R$. In figure (b), the big/small spots denote the A/B lattice sites, respectively, which are deep/shallow sites for \uparrow bosons. The boxes with red and blue dashed lines indicate the spatial regions covered by our 1×1 and 2×2 unit cell truncations.

In our work, the numerical simulations are based on an extended Bose-Hubbard (BH) model for the binary bosonic mixture in the SDHL. The construction of this extended Bose-Hubbard model is optimized in the sense that the amplitudes of leading-order neglected processes (for instance the density-induced tunneling) are minimized by the choice of optimal Wannier functions [34]. This optimization process gives rise to a single-band \ddagger BH model, in which only one Wannier function is assigned to each site, while higher-band states are solely used for constructing these optimized Wannier functions [34]. The resulting extended BH Hamiltonian contains not only the conventional terms, i.e. site offset energies, nearest-neighbor (NN) hopping and on-site interactions, but also next-to-nearest-neighbor (NNN) tunneling and NN interactions. The corresponding BH Hamiltonian reads:

$$\begin{aligned}
 H = & \sum_{i;\sigma} \varepsilon(i, \sigma) \hat{a}_{i,\sigma}^\dagger \hat{a}_{i,\sigma} - \sum_{\langle i,j \rangle; \sigma} J_1 \hat{a}_{i,\sigma}^\dagger \hat{a}_{j,\sigma} - \sum_{\langle\langle i,j \rangle\rangle; \sigma} J_2(i, \sigma) \hat{a}_{i,\sigma}^\dagger \hat{a}_{j,\sigma} \\
 & + \sum_{i;\sigma} U(i, \sigma) \hat{a}_{i,\sigma}^\dagger \hat{a}_{i,\sigma}^\dagger \hat{a}_{i,\sigma} \hat{a}_{i,\sigma} + \sum_{\langle i,j \rangle; \sigma} U_1 \hat{a}_{i,\sigma}^\dagger \hat{a}_{j,\sigma}^\dagger \hat{a}_{i,\sigma} \hat{a}_{j,\sigma} \\
 & + \sum_i W \hat{a}_{i,\uparrow}^\dagger \hat{a}_{i,\downarrow}^\dagger \hat{a}_{i,\uparrow} \hat{a}_{i,\downarrow} + \sum_{\langle i,j \rangle} W_1(i) \hat{a}_{i,\uparrow}^\dagger \hat{a}_{j,\downarrow}^\dagger \hat{a}_{i,\uparrow} \hat{a}_{j,\downarrow}.
 \end{aligned} \tag{2}$$

In the Hamiltonian, $\hat{a}_{i,\sigma}^{(\dagger)}$ denotes the annihilation (creation) operator of one boson of species $\sigma \in \{\uparrow, \downarrow\}$ at site i , and $\langle i, j \rangle$ ($\langle\langle i, j \rangle\rangle$) indicates the summation over all the NN

\ddagger Our approximation can equivalently be viewed as an extended two-band BH model if one regards the unit cells (A/B double wells) as elementary sites.

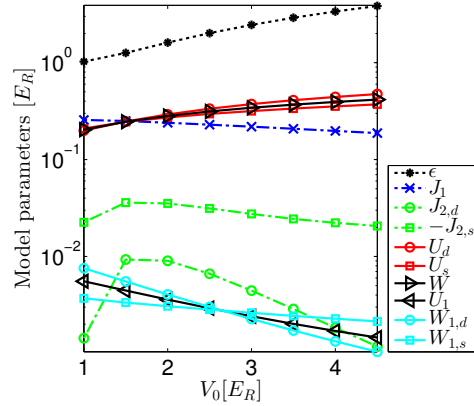


Figure 2. Parameters of the extended BH model as a function of the lattice depth, calculated according to [34] for the setup of the experiment [32].

(NNN) pairs. The first three terms of the Hamiltonian in equation (2) are the on-site energy, NN hopping and NNN hopping terms, respectively, and the following two terms are the intra-species on-site and NN interactions. The last two terms describe the inter-species on-site and NN interactions. Depending on the i -th site being deep or shallow for the σ species, the on-site energy $\varepsilon(i, \sigma)$ vanishes for deep sites and assumes a value of ε for shallow sites, and the NNN hopping matrix element $J_2(i, \sigma)$ becomes $J_{2,d}$ or $J_{2,s}$, respectively. Similarly, there are two in general different values U_d and U_s for the intra-species on-site interaction strength $U(i, \sigma)$. The NN inter-species interaction $W_1(i)$ takes the values $W_{1,d}$ (neighboring atoms in their respective deep sites) and $W_{1,s}$ (neighboring atoms in their respective shallow sites). The NN hopping matrix element J_1 , the NN intra-species interaction strength U_1 and the on-site inter-species interaction strength W are, however, site- and spin-independent. In the calculation of the amplitudes for the interaction processes, the intra- and inter-species scattering lengths are taken to be equal. Figure 2 shows the parameter values we work with as a function of the lattice depth V_0 .

Before turning to the many-body problem, let us briefly review the single particle properties of this system. The two species share the same single particle band structure, consisting of two branches as shown in figure 3. In contrast to what is found for a standard graphene-type honeycomb lattice, a gap between the two branches is opened due to the energy offset between A and B sites.

In our numerical simulations, we are limited to finite system sizes. The truncation domains we focus on here are a single (1×1) unit cell and 2×2 unit cells (cf. figure 1(b)), although we have also tried larger domains where however convergence is hard to ensure. For all truncation schemes, periodic boundary conditions are imposed. This results in an enhancement of the NN hopping strength J_1 by a factor of three for the 1×1 truncation compensating the reduced coordination number. In principle, the reduction of the coordination number can affect also the NN interaction processes, which, however, turn out to be negligibly small and are therefore not renormalized. Furthermore, we

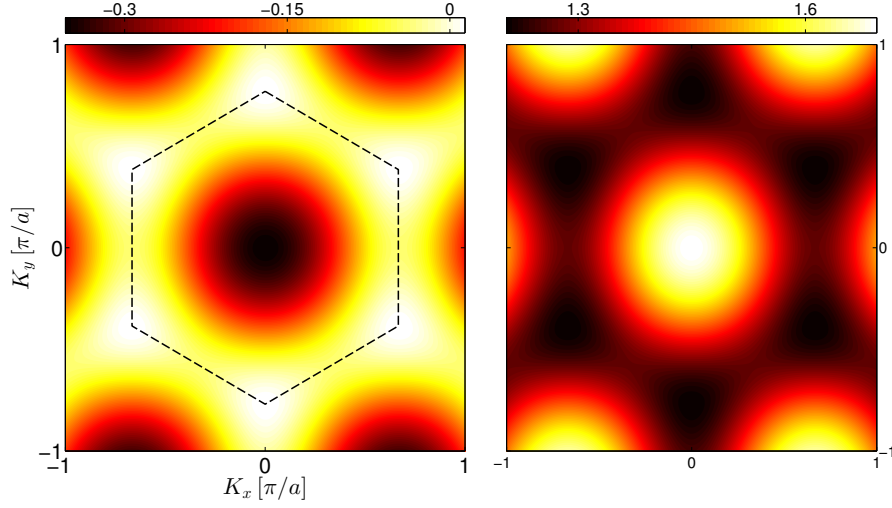


Figure 3. The single particle eigenenergy as a function of quasi-momenta for both the \uparrow and \downarrow bosons, calculated at $V_0 = 1.5E_R$. The left and right panels correspond to the lower and upper branch, respectively.

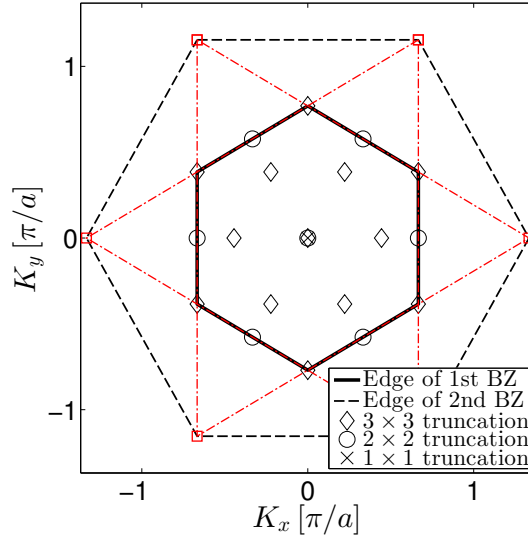


Figure 4. Edges of the first (solid line) and the second (dashed line) Brillouin zone in quasi-momentum space. Markers within the first Brillouin zone indicate the quasi-momenta sampled by our different truncation schemes (for illustration, we also show the 3×3 case here). The squares at the second Brillouin zone edges mark the first-order Bragg peaks, forming two equilateral triangles (\triangleleft and \triangleright) shown as dashed-dotted lines.

remark that the NNN hopping term is neglected when truncating to a single unit cell or 2×2 unit cells to avoid an artificial hopping from one site to itself. Finally, truncations in real space necessarily imply a corresponding discrete sampling of the continuous quasi-momentum space. In figure 4 we illustrate the sets of discrete quasi-momenta captured by our different real space truncation schemes.

3. Method

In this work, we apply ML-MCTDHB [35, 36] which is a highly flexible *ab initio* method for solving the time-dependent many-body Schrödinger equation for bosonic systems and in particular bosonic mixtures. The method is based on expanding the total wave function with respect to a time-dependent variationally optimized basis, which allows to capture the important correlation effects using a numerically feasible basis size. We employ imaginary time propagation in order to find the ground state of the binary mixture in the SDHL potential by means of ML-MCTDHB.

The power and flexibility of ML-MCTDHB mainly lies in the multi-layer ansatz for the total wave function. Going through this layer by layer, the total wavefunction is first expanded as

$$|\Psi(t)\rangle = \sum_{i,j=1}^M A_{i,j}(t) |\psi_i^\uparrow(t)\rangle |\psi_j^\downarrow(t)\rangle, \quad (3)$$

where the time-dependent basis for the σ species $\{|\psi_i^\sigma(t)\rangle\}_{i=1}^M$ consists of the so-called species-layer single particle functions (SPFs). These species layer SPFs are bosonic many-body states and as such expanded as

$$|\psi_i^\sigma(t)\rangle = \sum_{\mathbf{n}} B_{i;\mathbf{n}}^\sigma(t) |\mathbf{n}; t\rangle_\sigma. \quad (4)$$

Here $|\mathbf{n}; t\rangle_\sigma$ denotes the bosonic number state obtained by populating the time-dependent particle layer SPFs $\{|\varphi_j^\sigma(t)\rangle\}_{j=1}^m$ according to the occupation numbers $\mathbf{n} = (n_1, n_2, \dots, n_m)$ and the sum runs over all occupation numbers that add up to the number of σ bosons. In this work, we are only interested in balanced mixtures of N bosons per species. Finally, the particle layer SPFs, which constitute the instantaneous truncated basis within the single particle Hilbert space, are expanded in terms of the static Wannier states

$$|\varphi_j^\sigma(t)\rangle = \sum_l C_{j;l}^\sigma(t) |l_\sigma\rangle \quad (5)$$

where $|l_\sigma\rangle$ denotes the Wannier state of species σ in the l -th site of the SDHL lattice, as defined in Appendix A. In this recursive way the expansion coefficients $\{A_{i,j}, B_{i;\mathbf{n}}^\sigma, C_{i,j}^\sigma\}$ determine the total wave function, and their time evolution is governed by equations of motion [35, 36] obtained from a time-dependent variational principle [37, 38], which ensures the optimal choice of the SPF basis on all layers. Applying imaginary time propagation we thus obtain the expansion coefficients for the ground state of the bosonic mixture.

The numerical control parameters of the above expansions are the numbers M and m of species and particle layer SPFs of each species. Due to the symmetry between the two species, these numbers are taken to be independent of σ . In the limit of $M = m = 1$, the ML-MCTDHB expansion reduces to the mean-field ansatz, while the calculation becomes numerically exact for m equal to the number of lattice sites and $M = (N + m - 1)!/[N!(m - 1)!]$. Summarizing, for a given system size we have to

ensure that our simulations are converged with respect to the numbers of basis functions (M, m) such that all relevant correlations are captured.

4. Results

Having determined the ground state many-body wave function $|\Psi\rangle$ with the ML-MCTDHB method, we need to establish a link to time-of-flight measurements. Assuming that interactions do not play any role during the expansion of the binary Bose mixture, an ideal single shot absorption measurement after long time-of-flight effectively means to measure destructively the joint $(N_\downarrow, N_\uparrow)$ -particle free-space momentum distribution *before* the expansion [6]. In the following, we will focus on the first order Bragg peaks in the time-of-flight images: As indicated in figure 4, we group these six free-space momenta into two classes, namely the set of momenta in the triangle pointing to the right (left) denoted by $\triangleright = \{\mathbf{b}_1, \mathbf{b}_2, \mathbf{b}_3\}$ ($\triangleleft = \{-\mathbf{b}_1, -\mathbf{b}_2, -\mathbf{b}_3\}$). In Appendix A, we show that all elements of \triangleright (\triangleleft) are equivalent within our two-band approximation. Therefore, we may single out two representatives named $\mathbf{r} \in \triangleright$ and $\mathbf{l} \in \triangleleft$. Moreover, we denote the zero free-space momentum as \mathbf{k}_0 .

In the following, we will first discuss our findings for the experimental parameters of [32], in order to quantify how well this system is described by a mean-field approach. Afterwards, we will consider potentially relevant inter-species correlation effects, complementing the discussion of the experiment itself with some results for detuning energies between the shallow and deep lattice sites which are smaller than the experimentally implemented ones.

In both considerations, we find that the reduced one-body free-space momentum density of the species σ , $\rho_1^\sigma(\mathbf{k}) = \frac{1}{N_\sigma} \langle \Psi | \hat{\psi}_\sigma^\dagger(\mathbf{k}) \hat{\psi}_\sigma(\mathbf{k}) | \Psi \rangle$ with $\hat{\psi}_\sigma(\mathbf{k})$ denoting the annihilation operator of a free space momentum state \mathbf{k} , does not feature TSF properties. In fact, we have not found any numerical hints that the ground state $|\Psi\rangle$ might be degenerate. Therefore, $|\Psi\rangle$ features both a spin exchange and a six-fold rotation symmetry implying $\rho_1^\downarrow(\mathbf{q}) = \rho_1^\uparrow(\mathbf{q})$ with $\mathbf{q} \in \{\mathbf{r}, \mathbf{l}\}$ as well as $\rho_1^\sigma(\mathbf{r}) = \rho_1^\sigma(\mathbf{l})$ meaning that the average of species-selective histograms of $(N_\downarrow, N_\uparrow)$ -particle measurements over many shots does not give any TSF signatures.

4.1. Ground state properties in the parameter regime of the experiment

In this section we focus on the parameter values at which the experiment was performed. As explained above, numerical simulations have been performed for different lattice truncations. For each of these, the lattice depth was varied from weak to strong. In the 1×1 truncation, we consider 3 \uparrow and 3 \downarrow bosons, corresponding to a filling factor of 3 per unit cell for each species. For the 2×2 truncation, we consider a filling factor per unit cell being equal to unity for each species. Larger filling factors are computationally prohibitive for the 2×2 due to the slow convergence with respect to the number of SPFs on both layers as discussed in section 4.2.

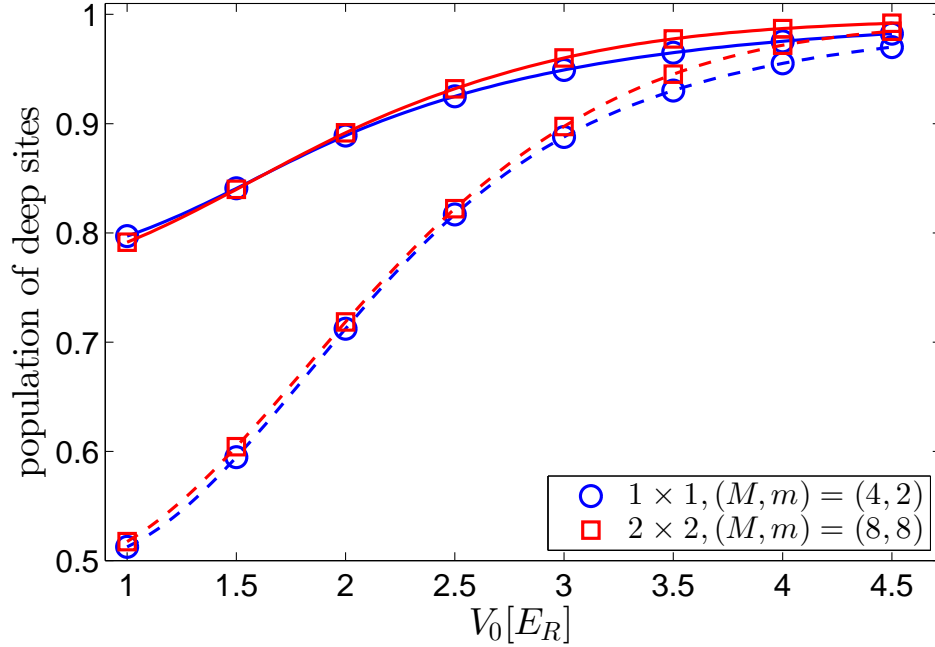


Figure 5. Population of \uparrow bosons in their deep sites as a function of the lattice depth V_0 , calculated within the 1×1 (blue lines) and 2×2 (red lines) truncations. The solid lines are calculated with the experimental parameters shown in figure 3, and the dashed lines are calculated for a smaller energy offset ε^* being discussed in section 4.2.

We start by discussing our results for the one-body density in position space. In figure 5 we present the population of \uparrow bosons in their corresponding deep sites, $\rho_A(\uparrow)$, as a function of the optical lattice depth. Due to the spin symmetry, the population of \downarrow bosons is given by $\rho_A(\uparrow) = \rho_B(\downarrow)$, while the σ species occupations at sites A and B add up to unity: $\rho_A(\sigma) + \rho_B(\sigma) = 1$. It can be seen that the \uparrow bosons already show a tendency to localize in the A sites in the weak lattice depth regime, and the localization becomes stronger as the lattice depth increases, following the increase of the state-dependent on-site energy offset ε . As the \downarrow bosons show the same tendency to be localized in their deep sites, *i.e.* the B sites, the spatial overlap between \uparrow and \downarrow bosons becomes vanishingly small for large V_0 . As a consequence, increasing V_0 leads to a suppression of inter-species correlations, as will be discussed below.

To quantify how close the system is to a mean-field state, we further calculate so-called depletions for various subsystems: Firstly focussing on a σ boson, the corresponding reduced one-body density operator is given by the partial trace of the total system state over all atoms but a single one of spin σ : $\hat{\rho}_1^\sigma = \text{Tr}_{\sigma;\text{part}} |\Psi\rangle\langle\Psi|$. Denoting the largest eigenvalue of $\hat{\rho}_1^\sigma$ as λ_p^σ , the depletion of a σ atom is defined as $d_\sigma = 1 - \lambda_p^\sigma$, which turns out to be independent of σ due to the spin-exchange symmetry, $d_\sigma \equiv d$. According to [39], d measures the degree of condensation of the σ bosons: d close to zero implies that intra-species correlations are negligible, *i.e.* all the σ bosons essentially occupy the same single particle state. In this way, $d \approx 0$ means that a mean-field ansatz for the

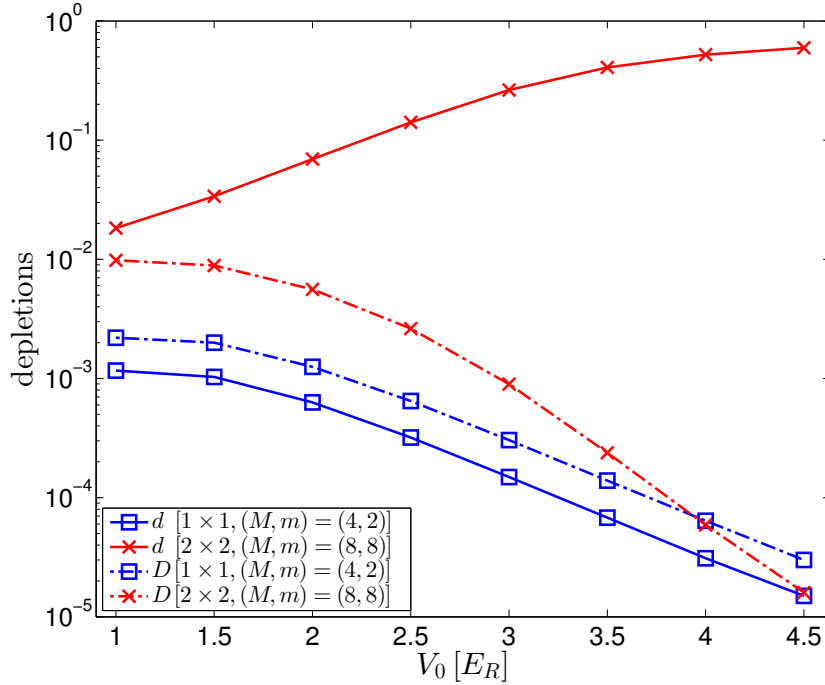


Figure 6. Species-level and particle-level depletions D (dashed-dotted lines) and d (solid lines) as a function of the lattice depth. The colours denote the results from different spatial truncations, with the corresponding (M, m) given in the legend.

state of the σ species is applicable, i.e. that one may set $m = 1$ in the wave function ansatz (3,4). Conversely, a significant value of d (< 1) indicates strong correlations between a σ boson and all the other atoms.

This concept can be transferred to the whole σ species whose reduced density operator is given by the partial trace of the total system state over the atoms of opposite spin: $\hat{\rho}_{\text{spec}}^\sigma = \text{Tr}_{\sigma; \text{spec}} |\Psi\rangle\langle\Psi|$. With λ_s^σ as its largest eigenvalue, we similarly define the depletion on the species layer as $D = 1 - \lambda_s^\sigma$ (which is again independent of the σ). This depletion measures how strongly the total state deviates from a single tensor product of a pure state for the \uparrow species and a pure state for the \downarrow species. For $D = 0$, this factorization holds exactly implying the validity of a mean-field ansatz ($M = 1$) on the species layer (3). Significant values of D (< 1) imply the presence of inter-species correlations resulting in a non-factorizable total wave function. We remark that the depletions d and D measure correlations in the system basis-independently.

Figure 6 shows the numerically obtained depletions D and d for our different spatial truncation schemes. Throughout, we find that the depletion D is very weak (below one percent) for all lattice depths considered, decreasing further for increasing V_0 . This latter trend is in agreement with the above discussion of the inter-species correlations (which are small throughout) being further suppressed due to a spatial separation of the \uparrow and \downarrow bosons. Turning to the depletion d , we find a qualitative difference between the 1×1 and 2×2 truncation schemes. While in the effectively one-dimensional 1×1 simulations, d is on the level of per mil or below, it assumes larger values in the 2×2

setup, starting from few percent for low V_0 and going up to around 0.5 for the largest lattice depth we consider, indicating fragmentation of the system on the level of a single species for deep lattices. This finding is consistent with approaching a Mott insulator phase for increasing V_0 , with the bosons of a species fully localizing in their respective deep sites. In the simulation with a single unit cell the fragmentation accompanying the localization cannot be captured since only a single deep site is available for each species. Overall, we observe that in the regime of small V_0 (where in the experiment the TSF was observed) there is no numerical evidence of sizable depletions. This indicates that a mean-field treatment of the system is indeed expected to give appropriate lowest order results, to which then quantum corrections apply. In the following we will turn to a detailed inspection of these beyond mean-field corrections, and their possible relation to the TSF signatures.

4.2. Interspecies correlation effects

In this section, we investigate inter-species correlation effects that potentially could give rise to properties characteristic for the TSF. From the discussion in the previous section it is generally expected that such correlations are small for the experimental parameter values of [32], but we will illustrate that they are enhanced in other regions of the parameter space.

One of the simplest quantities which may be sensitive to beyond mean-field signatures of the TSF properties is the inter-species free-space momentum g_2 -correlation function:

$$g_2^{\downarrow\uparrow}(\mathbf{q}_1, \mathbf{q}_2) = \frac{1}{N_\downarrow N_\uparrow} \frac{\langle \Psi | \hat{\psi}_\downarrow^\dagger(\mathbf{q}_1) \hat{\psi}_\uparrow^\dagger(\mathbf{q}_2) \hat{\psi}_\downarrow(\mathbf{q}_1) \hat{\psi}_\uparrow(\mathbf{q}_2) | \Psi \rangle}{\rho_1^\downarrow(\mathbf{q}_1) \rho_1^\uparrow(\mathbf{q}_2)}. \quad (6)$$

We note the spin exchange symmetry $g_2^{\downarrow\uparrow}(\mathbf{q}_2, \mathbf{q}_1) = g_2^{\downarrow\uparrow}(\mathbf{q}_1, \mathbf{q}_2)$ as well as the rotation symmetry $g_2^{\downarrow\uparrow}(\mathbf{r}, \mathbf{r}) = g_2^{\downarrow\uparrow}(\mathbf{l}, \mathbf{l})$. While $g_2^{\downarrow\uparrow}(\mathbf{q}_1, \mathbf{q}_2)$ equals unity in the mean-field approximation, correlations can result in inter-species bunching ($g_2^{\downarrow\uparrow}(\mathbf{q}_1, \mathbf{q}_2) > 1$) or antibunching ($g_2^{\downarrow\uparrow}(\mathbf{q}_1, \mathbf{q}_2) < 1$), which indicates that the spin exchange or six-fold rotation symmetry is stochastically violated in a *correlated manner* when detecting two bosons of opposite spin: If for instance $g_2^{\downarrow\uparrow}(\mathbf{r}, \mathbf{r})$ turns out to be larger than unity, we may conclude that, given one spin \uparrow boson has been destructively detected in one triangle, the probability for subsequently detecting a spin \downarrow boson in the very same triangle is enhanced compared to statistical independence. Moreover, we compare these correlations by introducing:

$$\delta g_2^{\downarrow\uparrow} = g_2^{\downarrow\uparrow}(\mathbf{r}, \mathbf{r}) - g_2^{\downarrow\uparrow}(\mathbf{r}, \mathbf{l}). \quad (7)$$

Finding $\delta g_2^{\downarrow\uparrow} < 0$ could consequently be interpreted as a manifestation of (P2) (see introduction) on the level of two-body measurements, i.e. that two bosons of different spin are more likely to be found in different triangles than in the same one.

Figure 7 depicts $\delta g_2^{\downarrow\uparrow}$ and, as an inset, also the individual addends $g_2^{\downarrow\uparrow}(\mathbf{r}, \mathbf{r})$ and $g_2^{\downarrow\uparrow}(\mathbf{r}, \mathbf{l})$ as a function of the lattice depth for various truncation sizes. We show the

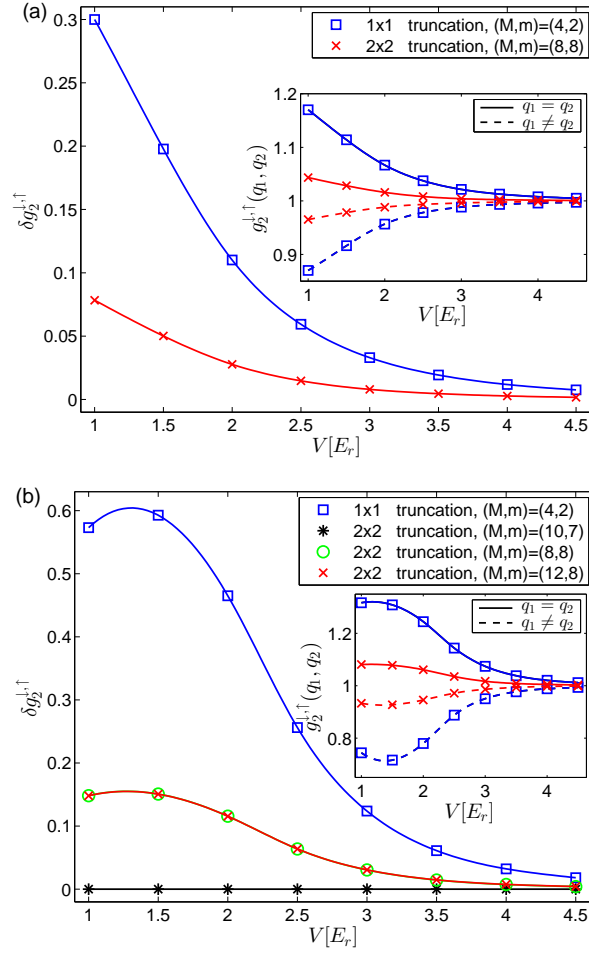


Figure 7. Inter-species correlation difference $\delta g_2^{\downarrow, \uparrow}$ as a function of lattice depth, for (a) the experimental value of the energy offset as shown in figure 2 and (b) the by one recoil energy reduced ε^* . In the upper panel, the blue and red lines are for 1×1 and 2×2 truncations, respectively, with the corresponding (M, m) given in the legend. In the lower panel, results for 2×2 truncation with different (M, m) are also given. The insets in both panels depict $g_2^{\downarrow, \uparrow}(\mathbf{q}_2, \mathbf{q}_1)$ with $\mathbf{q}_2 = \mathbf{q}_1$ (solid line) and $\mathbf{q}_2 \neq \mathbf{q}_1$ (dashed line).

quantities for the experimental parameters, which as expected are small since the system is in the mean field regime. For the sake of illustration, we have also included results for the on-site energy detuning $\varepsilon^* = \varepsilon - E_R$, which is reduced by one recoil energy compared to the value of the experiment [32] while all other parameters in the Hamiltonian are kept fixed. It can be observed that the inter-species correlations are enhanced for the reduced detuning ε^* in comparison to the results for ε . Understandably, reducing the energy difference between the species-dependent deep and shallow sites reduces the bosons' tendency to separate into the sublattices. In turn, the inter-species spatial overlap is larger, enabling the emergence of correlations. Enhancement of the correlations is also observed when increasing the inter-species interaction (results not shown).

Notably, the values of both $|\delta g_2^{\downarrow, \uparrow}|$ and $|g_2^{\downarrow, \uparrow}(\mathbf{q}_1, \mathbf{q}_2) - 1|$ are largest for the single unit

cell truncation where the simulated system is effectively one-dimensional, while they tend to decrease when going to larger truncation sizes where the true two-dimensional structure of the extended lattice is correctly taken into account. The magnitude of correlations is reduced for larger truncation sizes as more energetically favourable states are included in the discrete sampling of the quasi-momentum space: As shown in Appendix B, a non-vanishing $\delta g_2^{\downarrow\uparrow}$ requires a finite coherence between the single particle ground and highest excited state within the single band approximation. If now energetically lower lying states become available when increasing the truncation size, atoms generically tend to occupy these states and thereby reduce the inter-branch coherences related to $\delta g_2^{\downarrow\uparrow}$.

Importantly, for the two different values of the energy offset, we only observe positive values of $\delta g_2^{\downarrow\uparrow}$, indicating that due to inter-species correlations one \uparrow and one \downarrow boson slightly tend to concentrate in the same triangle, in contrast to (P2). Thus, even if the weak inter-species correlations of this kind are taken into consideration (and as we have seen they may become more relevant in regions of the parameter space away from the experimental values) we find no hint that they can cause the emergence of a (P2) signature.

We furthermore remark that the correlation measure $\delta g_2^{\downarrow\uparrow}$ converges slowly with the number of SPFs: It can be inferred from figure 7 that one has to provide as many particle layer SPFs as there are sites, which corresponds to the numerically exact limit with respect to the particle layer basis and stems from the fact that coherences between the energetically most separated single particle eigenstates must be resolved for having $\delta g_2^{\downarrow\uparrow}$ non-vanishing (cf. Appendix B).

So far, we have only discussed two-body correlation properties. In some situations, however, it can be difficult to generalize the results for two-body observables to N particle measurements (cf. e.g. the discussion [40–43]). For this reasons, we evaluate here the joint probability distribution for detecting n_0^σ , n_\triangleleft^σ , n_\triangleright^σ bosons of spin σ at zero free-space momentum, in \triangleleft , in \triangleright , respectively: $P(n_0^\uparrow, n_\triangleleft^\uparrow, n_\triangleright^\uparrow; n_0^\downarrow, n_\triangleleft^\downarrow, n_\triangleright^\downarrow)$. Restricting ourselves to the 1×1 truncation and bearing in mind that the states within \triangleleft (\triangleright) are equivalent within the lowest band approximation (cf. Appendix A), this probability distribution is given by:

$$P(n_0^\uparrow, n_\triangleleft^\uparrow, n_\triangleright^\uparrow; n_0^\downarrow, n_\triangleleft^\downarrow, n_\triangleright^\downarrow) = \frac{1}{16} \prod_{\sigma \in \{\uparrow, \downarrow\}} (n_\triangleleft^\sigma + 1)(n_\triangleleft^\sigma + 2)(n_\triangleright^\sigma + 1)(n_\triangleright^\sigma + 2) \quad (8)$$

$$\times \tilde{P}(n_0^\uparrow, n_\triangleleft^\uparrow, n_\triangleright^\uparrow; n_0^\downarrow, n_\triangleleft^\downarrow, n_\triangleright^\downarrow).$$

Here, $\tilde{P}(n_0^\uparrow, n_1^\uparrow, n_{\mathbf{r}}^\uparrow; n_0^\downarrow, n_1^\downarrow, n_{\mathbf{r}}^\downarrow)$ refers to the probability for finding n_0^σ , n_1^σ , $n_{\mathbf{r}}^\sigma$ bosons of spin σ in the free-space momentum states \mathbf{k}_0 , \mathbf{l} , \mathbf{r} , respectively, which can be calculated in terms of an expectation value of the operators $\hat{\psi}_\sigma^{(\dagger)}(\mathbf{k})$ (cf. (B.1) for $\mathbf{k} = \mathbf{l}, \mathbf{r}$).

In figure 8, the probability distribution $P(n_0^\uparrow, n_\triangleleft^\uparrow, n_\triangleright^\uparrow; n_0^\downarrow, n_\triangleleft^\downarrow, n_\triangleright^\downarrow)$ is depicted for the reduced energy offset ε^* and $V_0 = 1E_R$ as well as $V_0 = 4.5E_R$. We clearly see that detection events with two or three bosons per species in \mathbf{k}_0 dominate in probability for the shallow lattice while for the deep lattice the probability is largest for detecting

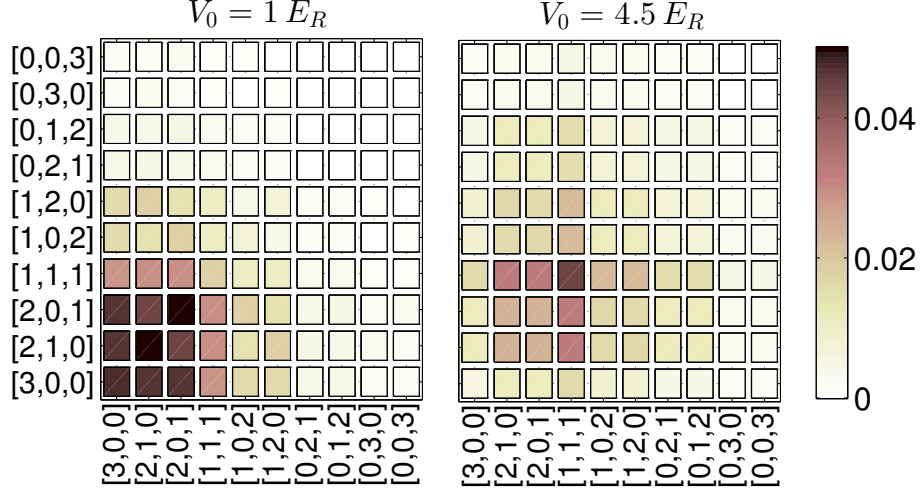


Figure 8. The joint probability for finding $[n_0^\uparrow, n_\triangleright^\uparrow, n_\triangleleft^\uparrow]$ bosons of spin \uparrow (x-axis) and $[n_0^\downarrow, n_\triangleright^\downarrow, n_\triangleleft^\downarrow]$ bosons of spin \downarrow (y axis) in $\mathbf{k}_0, \triangleright, \triangleleft$, respectively, for the energy offset ε^* and $V_0 = 1E_R$ (left) as well as $V_0 = 4.5E_R$ (right).

one σ boson in \mathbf{k}_0 , another one in \triangleleft and the third one in \triangleright . Moreover, we observe for the deep lattice that the four combinations of finding two \uparrow and two \downarrow bosons in \mathbf{k}_0 and the remaining \uparrow and \downarrow boson in $\triangleleft / \triangleright$ are of the same probability indicating the absence of inter-species two-body correlations, i.e. $g_2^{\downarrow, \uparrow}(\mathbf{q}_1, \mathbf{q}_2) \approx 1$ for $\mathbf{q}_i \in \{\mathbf{r}, \mathbf{l}\}$. In contrast to this, the presence of inter-species correlations can be witnessed for the shallow lattice: The largest probability $P(2, 1, 0; 2, 1, 0) = P(2, 0, 1; 2, 0, 1)$ relates to detecting two bosons per species in \mathbf{k}_0 and the remaining two bosons of opposite spin in the very same triangle, which is consistent with $\delta g_2^{\downarrow, \uparrow} > 0$ indicating the bunching of bosons of opposite spin in the same triangle. Therefore, also the joint probability distribution gives a slight inter-species bunching effect opposite to (P2). In view of (P1), we have also considered the marginal probability distribution of finding $n_0^\uparrow, n_\triangleleft^\uparrow, n_\triangleright^\uparrow$ bosons of spin \uparrow at zero free-space momentum, in \triangleleft , in \triangleright - irrespectively of the state in which the \downarrow bosons are found (plot not shown). Both this marginal probability distribution and the full probability distribution indicate that the first order Bragg peak triangles are most likely either unoccupied or occupied by a single boson. This finding can in principle be related to an asymmetric occupation of the triangles within one species, i.e. (P1). However, we cannot prove this tendency as this would require to consider more than three bosons per species, i.e. going at least to the 2×2 truncation.

5. Conclusions and discussion

We have studied the ground state properties of a binary bosonic mixture confined in a state-dependent honeycomb lattice for different values of the lattice depth. Our

results show that in the parameter regime related to the experimental setup in [32], the system can be relatively well described by a mean-field approximation, and only small corrections in the form of inter-species quantum correlations are observed. No indications of a ground state degeneracy are found. We study possible relations of the correlation effects beyond mean-field to potential signatures of the TSF and find that the correlations can indeed modify the population of the first order Bragg peaks after time-of-flight. The specific properties characteristic of the twisted superfluid are however not observed in our simulations. Our results imply that the emergence of the twisted superfluid cannot be explained by taking into account quantum corrections within the lowest-band extended Bose-Hubbard Hamiltonian. The most severe restrictions of our investigations are the finite system size, limiting us to a regime far away from an infinitely extended lattice. This truncation in real space implies a discrete selection of quasi-momenta as illustrated in figure 4, which does not capture the long wavelength excitations of the system. Given the slow convergence of the correlation properties with respect to the number of basis functions (M, m) , going to larger system sizes is computationally prohibitive. Furthermore, our model Hamiltonian neglects higher band effects whose importance for the twisted superfluid effect therefore remains as an open question. One may also speculate that neglected processes in the lowest-band extended BH model, such as the density-induced tunneling or pair tunneling terms, may be of importance in the emergence of the twisted superfluid.

Acknowledgments

P.S., K.S. and L.C. gratefully acknowledge funding by the Deutsche Forschungsgemeinschaft in the framework of the SFB 925 “Light induced dynamics and control of correlated quantum systems”. S.K. and J.S. gratefully acknowledge a scholarship by the Studienstiftung des deutschen Volkes.

Appendix A. Transformation of single particle basis

Due to the local character of the BH Hamiltonian (2), our simulations are performed in real space. Afterwards the result has to be transformed into the free space momentum basis in order to establish a link to the time-of-flight measurements. Moreover, one can relate certain inter-species correlations in the free momentum space to coherences between quasi-momentum states as shown in Appendix B. For these reasons, we provide the transformations between the Wannier, quasi-momentum and free-space momentum bases, which are relevant for this work.

Let $w_{A/B}^\sigma(\mathbf{x})$ denote the Wannier function of species σ for a site of type A/B centered at position $\mathbf{x} = \mathbf{0}$ as constructed in [34]. Then the Wannier basis $\{|\mathbf{R}\rangle_{\sigma,A}, |\mathbf{R}\rangle_{\sigma,B}\}$ can be obtained by Bravais translations

$$\langle \mathbf{x} | \mathbf{R} \rangle_{\sigma,A} = w_A^\sigma(\mathbf{x} - \mathbf{R}), \quad \langle \mathbf{x} | \mathbf{R} \rangle_{\sigma,B} = w_B^\sigma(\mathbf{x} - \mathbf{R} - \mathbf{r}). \quad (\text{A.1})$$

§ Note that in the main text the compact notation $|j\rangle_\sigma$ with a joint site index j has been employed.

Here, $\mathbf{R} = n_1 \mathbf{R}_1 + n_2 \mathbf{R}_2$ with $n_1, n_2 \in \mathbb{Z}$ refers to a site of the A sublattice, and the Bravais vectors of this hexagonal lattice are given by $\mathbf{R}_1 = \lambda(\frac{1}{\sqrt{3}}, \frac{1}{3})$ and $\mathbf{R}_2 = \lambda(0, \frac{2}{3})$. The relative distance between an A and a B site within a unit cell reads $\mathbf{r} = \lambda(-\frac{\sqrt{3}}{9}, -\frac{1}{3})$, with norm $|\mathbf{r}| = a$. We note the relation between the Bravais and the reciprocal lattice vectors $\mathbf{R}_i \cdot \mathbf{b}_j = 2\pi\delta_{ij}$ for $i = 1, 2$.

Projecting the Wannier basis onto free-space momentum states, i.e. plane waves $\langle \mathbf{x} | \mathbf{k} \rangle \propto \exp(i\mathbf{k}\mathbf{x})$, provides the following matrix for the transformation from the Wannier to the free-momentum basis:

$$\langle \mathbf{k} | \mathbf{R} \rangle_{\sigma, A} \propto e^{-i\mathbf{k}\mathbf{R}} \phi_A^\sigma(\mathbf{k}), \quad \langle \mathbf{k} | \mathbf{R} \rangle_{\sigma, B} \propto e^{-i\mathbf{k}(\mathbf{R}-\mathbf{r})} \phi_B^\sigma(\mathbf{k}) \quad (\text{A.2})$$

where we have defined the Fourier transformation of $w_{A/B}^\sigma(\mathbf{x})$ as

$$\phi_{A/B}^\sigma(\mathbf{k}) = \frac{1}{2\pi} \int d^2x w_{A/B}^\sigma(\mathbf{x}) e^{-i\mathbf{k}\mathbf{x}}. \quad (\text{A.3})$$

We note that $\langle \mathbf{k} | \mathbf{R} \rangle_{\sigma, A}$ and $\langle \mathbf{k} | \mathbf{R} \rangle_{\sigma, B}$ feature a phase factor difference of $\exp(-i\mathbf{k}\mathbf{r})$, due to the finite separation of A and B sites within the same unit cell. Relation (A.2) can be used for transforming the quasi-momentum states $|\mathbf{Q}\rangle_{\sigma, A/B}$ (which we label with capital letters \mathbf{Q} to distinguish them from free-space momentum states):

$$|\mathbf{Q}\rangle_{\sigma, A/B} \propto \sum_{\mathbf{R}} e^{i\mathbf{Q}\mathbf{R}} |\mathbf{R}\rangle_{\sigma, A/B}, \quad (\text{A.4})$$

to free-space momentum states $|\mathbf{k}\rangle$. Projecting onto $|\mathbf{k}\rangle$ and employing plane wave orthogonality results in:

$$\langle \mathbf{k} | \mathbf{Q} \rangle_{\sigma, A} \propto \phi_A^\sigma(\mathbf{k}) \sum_{\mathbf{R}} e^{i(\mathbf{Q}-\mathbf{k})\mathbf{R}} \propto \phi_A^\sigma(\mathbf{k}) \delta_{\mathcal{Q}(\mathbf{k}), \mathbf{Q}} \quad (\text{A.5})$$

where we have introduced the map \mathcal{Q} that projects its argument vector into the first Brillouin zone, i.e. shifts it by an appropriate reciprocal lattice vector. Correspondingly, we have $\langle \mathbf{k} | \mathbf{Q} \rangle_{\sigma, B} \propto \exp(-i\mathbf{k}\mathbf{r}) \phi_B^\sigma(\mathbf{k}) \delta_{\mathcal{Q}(\mathbf{k}), \mathbf{Q}}$.

Using these relations together with the orthonormality and assumed completeness of the lowest band Bloch basis, we find the following representation of free momentum states in terms of the quasi-momentum basis:

$$|\mathbf{k}\rangle_\sigma \simeq \mathcal{N} \left[\phi_A^\sigma(\mathbf{k})^* |\mathcal{Q}(\mathbf{k})\rangle_{\sigma, A} + e^{i\mathbf{k}\mathbf{r}} \phi_B^\sigma(\mathbf{k})^* |\mathcal{Q}(\mathbf{k})\rangle_{\sigma, B} \right], \quad (\text{A.6})$$

where \mathcal{N} is a normalization constant. In this expression, we have explicitly introduced the species index on the left hand side. We emphasize that the representation (A.6) is an identity only within the truncation to the lowest band and should be read as follows: $|\mathbf{k}\rangle_\sigma$ is given by the expression on the right hand side plus a remainder which, however, is orthogonal to our truncated Hilbert space and as such can be neglected when evaluating the simulation results. In particular, we note that (A.6) is not in conflict with e.g. the orthogonality of free-space momentum states.

Since the first order Bragg peaks in the long time-of-flight absorption measurements are particularly relevant in view of the TSF properties, we concretise the transformation (A.6) for these free-space momenta here. The Wannier functions $w_{A/B}^\sigma$ are real

functions with three-fold rotational symmetry and possess the symmetry $w_{A/B}^\uparrow(\mathbf{x}) = w_{B/A}^\downarrow(-\mathbf{x})$ under spin exchange, which greatly reduces the number of independent Fourier coefficients. In particular we find the identities for $i, j, k, l \in \{1, 2\}$:

$$\begin{aligned}\phi_A^\uparrow(\mathbf{b}_i) &= \phi_A^\uparrow(-\mathbf{b}_j)^* = \phi_B^\downarrow(\mathbf{b}_k)^* = \phi_B^\downarrow(-\mathbf{b}_l) =: \phi_A, \\ \phi_B^\uparrow(\mathbf{b}_i) &= \phi_B^\uparrow(-\mathbf{b}_j)^* = \phi_A^\downarrow(\mathbf{b}_k)^* = \phi_A^\downarrow(-\mathbf{b}_l) =: \phi_B.\end{aligned}\tag{A.7}$$

Thus, we can restrict to arbitrary representatives $\mathbf{r} \in \triangleright$ and $\mathbf{l} \in \triangleleft$ and find using (A.6):

$$\begin{aligned}|\mathbf{r}\rangle_\uparrow &\simeq \tilde{\mathcal{N}} (\phi_A^* |\mathbf{Q} = \mathbf{0}\rangle_{\uparrow,A} + \phi_B^* e^{-2i\pi/3} |\mathbf{Q} = \mathbf{0}\rangle_{\uparrow,B}), \\ |\mathbf{l}\rangle_\uparrow &\simeq \tilde{\mathcal{N}} (\phi_A |\mathbf{Q} = \mathbf{0}\rangle_{\uparrow,A} + \phi_B e^{2i\pi/3} |\mathbf{Q} = \mathbf{0}\rangle_{\uparrow,B}), \\ |\mathbf{r}\rangle_\downarrow &\simeq \tilde{\mathcal{N}} (\phi_B |\mathbf{Q} = \mathbf{0}\rangle_{\downarrow,A} + \phi_A e^{-2i\pi/3} |\mathbf{Q} = \mathbf{0}\rangle_{\downarrow,B}), \\ |\mathbf{l}\rangle_\downarrow &\simeq \tilde{\mathcal{N}} (\phi_B^* |\mathbf{Q} = \mathbf{0}\rangle_{\downarrow,A} + \phi_A^* e^{2i\pi/3} |\mathbf{Q} = \mathbf{0}\rangle_{\downarrow,B}),\end{aligned}\tag{A.8}$$

where $\tilde{\mathcal{N}}$ denotes a normalization constant and the \simeq symbol has to be understood as in (A.6).

Appendix B. Free-space momentum correlations and quasi-momentum coherences

In this appendix, we establish a link between the correlation function difference $\delta g_2^{\downarrow,\uparrow}$ and inter-branch coherences given a real-valued total wave function in quasi-momentum space: By means of the transformation (A.9), we may express the annihilation operator for a σ boson in the free space momentum $\mathbf{q} \in \{\mathbf{r}, \mathbf{l}\}$ as

$$\hat{\psi}_\sigma(\mathbf{q}) \simeq {}_\sigma\langle \mathbf{q} | \mathbf{Q} = \mathbf{0} \rangle_{\sigma,A} \hat{\alpha}_\sigma + {}_\sigma\langle \mathbf{q} | \mathbf{Q} = \mathbf{0} \rangle_{\sigma,B} \hat{\beta}_\sigma,\tag{B.1}$$

where $\hat{\alpha}_\sigma, \hat{\beta}_\sigma$ refer to the annihilation operators corresponding to $|\mathbf{Q} = \mathbf{0}\rangle_{\sigma,A}, |\mathbf{Q} = \mathbf{0}\rangle_{\sigma,B}$, respectively. The ground state being non-degenerate (as observed numerically) implies $\langle \hat{\psi}_\uparrow^\dagger(\mathbf{q}) \hat{\psi}_\uparrow(\mathbf{q}) \rangle = \langle \hat{\psi}_\downarrow^\dagger(\mathbf{q}) \hat{\psi}_\downarrow(\mathbf{q}) \rangle \equiv \bar{n}$. Introducing $\Theta = \phi_A^* \phi_B e^{2i\pi/3}$, we find:

$$\begin{aligned}\bar{n}^2 \delta g_2^{\downarrow,\uparrow} &= \langle \hat{\psi}_\downarrow^\dagger(\mathbf{r}) \hat{\psi}_\downarrow(\mathbf{r}) [\hat{\psi}_\uparrow^\dagger(\mathbf{r}) \hat{\psi}_\uparrow(\mathbf{r}) - \hat{\psi}_\uparrow^\dagger(\mathbf{l}) \hat{\psi}_\uparrow(\mathbf{l})] \rangle \\ &= 2i\tilde{\mathcal{N}}^2 \text{Im}(\Theta) \langle \hat{\psi}_\downarrow^\dagger(\mathbf{r}) \hat{\psi}_\downarrow(\mathbf{r}) [\hat{\alpha}_\uparrow^\dagger \hat{\beta}_\uparrow - \hat{\beta}_\uparrow^\dagger \hat{\alpha}_\uparrow] \rangle \\ &= -2\tilde{\mathcal{N}}^4 \text{Im}(\Theta)^2 \langle [\hat{\alpha}_\downarrow^\dagger \hat{\beta}_\downarrow - \hat{\beta}_\downarrow^\dagger \hat{\alpha}_\downarrow] [\hat{\alpha}_\uparrow^\dagger \hat{\beta}_\uparrow - \hat{\beta}_\uparrow^\dagger \hat{\alpha}_\uparrow] \rangle.\end{aligned}\tag{B.2}$$

For the last identity, we have made use of the assumption that the total wave function of our non-degenerate ground state can be chosen to be real-valued with respect to the quasi-momentum basis.

From the single particle band structure in figure 3, we may infer that the single particle ground state and the energetically highest excited single particle state of a σ boson are superpositions of $|\mathbf{Q} = \mathbf{0}\rangle_{\sigma,A}$ and $|\mathbf{Q} = \mathbf{0}\rangle_{\sigma,B}$. Therefore, $\delta g_2^{\downarrow,\uparrow}$ can be expressed in terms of annihilation and creation operators of these two eigenstates, which can shed a light on the magnitude of $\delta g_2^{\downarrow,\uparrow}$ from an energetic viewpoint. In the following, we

denote the annihilation operators of a σ boson in the single particle ground and highest excited state as $\hat{\psi}_{\sigma,g}$ and $\hat{\psi}_{\sigma,e}$, respectively. Without loss of generality, we may write:

$$\begin{cases} \hat{\psi}_{\uparrow,g} = \sin(\theta)\hat{\alpha}_{\uparrow} + \cos(\theta)\hat{\beta}_{\uparrow} \\ \hat{\psi}_{\uparrow,e} = \cos(\theta)\hat{\alpha}_{\uparrow} - \sin(\theta)\hat{\beta}_{\uparrow} \end{cases} \quad \begin{cases} \hat{\psi}_{\downarrow,g} = \sin(\theta)\hat{\beta}_{\downarrow} + \cos(\theta)\hat{\alpha}_{\downarrow} \\ \hat{\psi}_{\downarrow,e} = \cos(\theta)\hat{\beta}_{\downarrow} - \sin(\theta)\hat{\alpha}_{\downarrow} \end{cases} \quad (\text{B.3})$$

The value of θ is then determined by ε , J_1 , and $J_{2,d/s}$. Consequently, we obtain:

$$\bar{n}^2 \delta g_2^{\downarrow,\uparrow} = -2\tilde{\mathcal{N}}^4 \text{Im}(\Theta)^2 \langle [\hat{\psi}_{\downarrow,g}^\dagger \hat{\psi}_{\downarrow,e} - \hat{\psi}_{\downarrow,e}^\dagger \hat{\psi}_{\downarrow,g}] [\hat{\psi}_{\uparrow,g}^\dagger \hat{\psi}_{\uparrow,e} - \hat{\psi}_{\uparrow,e}^\dagger \hat{\psi}_{\uparrow,g}] \rangle. \quad (\text{B.4})$$

This result clearly shows that the magnitude of $\delta g_2^{\downarrow,\uparrow}$ is controlled by coherences in the inter-species reduced two-body density operator with respect to the single particle eigenstates of lowest and highest eigenenergy.

References

- [1] Anderson M H, Ensher J R, Matthews M R, Wieman C E and Cornell E A 1995 *Science* **269** 198
- [2] Bradley C C, Sackett C A, Tollett J J and Hulet R G 1995 *Phys. Rev. Lett.* **75** 1687
- [3] Davis K B, Mewes M O, Andrews M R, van Druten N J, Durfee D S, Kurn D M and Ketterle W 1995 *Phys. Rev. Lett.* **75** 3969
- [4] Bloch I 2005 *Nat. Phys.* **1** 23
- [5] Windpassinger P and Sengstock K 2013 *Rep. Prog. Phys.* **76** 086401
- [6] Bloch I, Dalibard J and Zwerger W 2008 *Rev. Mod. Phys.* **80** 885
- [7] Chin C, Grimm R, Julienne P and Tiesinga E 2010 *Rev. Mod. Phys.* **82** 1225
- [8] Köhler T, Góral K and Julienne P S 2006 *Rev. Mod. Phys.* **78** 1311
- [9] Olshanii M 1998 *Phys. Rev. Lett.* **81** 938
- [10] Bergeman T, Moore M G and Olshanii M 2003 *Phys. Rev. Lett.* **91** 163201
- [11] Kim J I, Melezhik V S and Schmelcher P 2006 *Phys. Rev. Lett.* **97** 193203
- [12] Melezhik V S, Kim J I and Schmelcher P 2007 *Phys. Rev. A* **76** 053611
- [13] Saeidian S, Melezhik V S and Schmelcher P 2008 *Phys. Rev. A* **77** 042721
- [14] Schützhold R, Uhlmann M, Xu Y and Fischer U R 2006 *Phys. Rev. Lett.* **97** 200601
- [15] Dziarmaga J and Rams M M 2010 *New J. Phys.* **12** 055007
- [16] del Campo A, Retzker A and Plenio M B 2011 *New J. Phys.* **13** 083022
- [17] Hung C L, Gurarie V and Chin C 2013 *Science* **341** 1213
- [18] Greiner M, Mandel O, Esslinger T, Hansch T W and Bloch I 2002 *Nature* **415** 39
- [19] Köhl M, Moritz H, Stöferle T, Schori C and Esslinger T 2005 *J. Low Temp. Phys.* **138** 635
- [20] Roati G, D'Errico C, Fallani L, Fattori M, Fort C, Zaccanti M, Modugno G, Modugno M and Inguscio M 2008 *Nature* **453** 895
- [21] Modugno G 2010 *Rep. Prog. Phys.* **73** 102401
- [22] Palmer R N, Klein A and Jaksch D 2008 *Phys. Rev. A* **78** 013609
- [23] Catani J, De Sarlo L, Barontini G, Minardi F and Inguscio M 2008 *Phys. Rev. A* **77** 011603
- [24] He L, Li Y, Altman E and Hofstetter W 2012 *Phys. Rev. A* **86** 043620
- [25] Taglieber M, Voigt A C, Aoki T, Hänsch T W and Dieckmann K 2008 *Phys. Rev. Lett.* **100** 010401
- [26] Tiecke T G, Goosen M R, Ludewig A, Gensemer S D, Kraft S, Kokkelmans S J J M F and Walraven J T M 2010 *Phys. Rev. Lett.* **104** 053202
- [27] Ospelkaus C, Ospelkaus S, Sengstock K and Bongs K 2006 *Phys. Rev. Lett.* **96** 020401
- [28] Ospelkaus C, Ospelkaus S, Humbert L, Ernst P, Sengstock K and Bongs K 2006 *Phys. Rev. Lett.* **97** 120402
- [29] Ospelkaus S, Ospelkaus C, Humbert L, Sengstock K and Bongs K 2006 *Phys. Rev. Lett.* **97** 120403
- [30] Snoek M, Titvinidze I, Bloch I and Hofstetter W 2011 *Phys. Rev. Lett.* **106** 155301
- [31] Heinze J, Götze S, Krauser J S, Hundt B, Fläschner N, Lühmann D S, Becker C and Sengstock K 2011 *Phys. Rev. Lett.* **107** 135303

- [32] Soltan-Panahi P, Lühmann D S, Struck J, Windpassinger P and Sengstock K 2012 *Nat. Phys.* **8** 71
- [33] Choudhury S and Mueller E J 2013 *Phys. Rev. A* **87** 033621
- [34] Lühmann D S, Jörgensen O, Weinberg M, Simonet J, Soltan-Panahi P and Sengstock K 2014 *arXiv* **1401.5961**
- [35] Krönke S, Cao L, Vendrell O and Schmelcher P 2013 *New J. Phys.* **15** 063018
- [36] Cao L, Krönke S, Vendrell O and Schmelcher P 2013 *J. Chem. Phys.* **139** 134103
- [37] McLachlan A 1963 *Mol. Phys.* **8** 39
- [38] Broeckhove J, Lathouwers L, Kesteloot E and Leuven P V 1988 *Chem. Phys. Lett.* **149** 547
- [39] Penrose O and Onsager L 1956 *Phys. Rev.* **104** 576
- [40] Mishmash R V and Carr L D 2009 *Phys. Rev. Lett.* **103** 140403
- [41] Dziarmaga J, Deuar P and Sacha K 2010 *Phys. Rev. Lett.* **105** 018903
- [42] Mishmash R V and Carr L D 2010 *Phys. Rev. Lett.* **105** 018904
- [43] Delande D and Sacha K 2014 *Phys. Rev. Lett.* **112** 040402